Neural Regeneration Research

Home
Current issue
Instructions
Submit article

Detecting white matter alterations in multiple sclerosis using advanced diffusion magnetic resonance imaging

Sourajit M. Mustafi,[1] Jaroslaw Harezlak,[2] Chandana Kodiweera,[3] Jennifer S. Randolph,[4] James C. Ford,[4] Heather A. Wishart,[4] and Yu-Chien Wu, PhD, DABMP[1,3,*]

[1]Department of Radiology and Imaging Sciences, Indiana University School of Medicine, Indianapolis, IN, USA
[2]Department of Epidemiology and Biostatistics, School of Public Health, Indiana University, Bloomington, IN, USA
[3]Department of Psychological and Brain Sciences and Dartmouth Brain Imaging Center, Dartmouth College, Hanover, NH, USA
[4]Department of Psychiatry, Geisel School of Medicine at Dartmouth, Lebanon, NH, USA
*Correspondence to: Yu-Chien Wu, yucwu@iu.edu.

Abstract

Multiple sclerosis is a neurodegenerative and inflammatory disease, a hallmark of which is demyelinating lesions in the white matter. We hypothesized that alterations in white matter microstructures can be non-invasively characterized by advanced diffusion magnetic resonance imaging. Seven diffusion metrics were extracted from hybrid diffusion imaging acquisitions *via* classic diffusion tensor imaging, neurite orientation dispersion and density imaging, and q-space imaging. We investigated the sensitivity of the diffusion metrics in 36 sets of regions of interest in the brain white matter of six female patients (age 52.8 ± 4.3 years) with multiple sclerosis. Each region of interest set included a conventional T2-defined lesion, a matched perilesion area, and normal-appearing white matter. Six patients with multiple sclerosis ($n = 5$) or clinically isolated syndrome ($n = 1$) at a mild to moderate disability level were recruited. The patients exhibited microstructural alterations from normal-appearing white matter transitioning to perilesion areas and lesions, consistent with decreased tissue restriction, decreased axonal density, and increased classic diffusion tensor imaging diffusivity. The findings suggest that diffusion compartment modeling and q-space analysis appeared to be sensitive for detecting subtle microstructural alterations between perilesion areas and

normal-appearing white matter.

Keywords: *multiple sclerosis*, *hybrid diffusion imaging*, *NODDI*, *diffusion tensor imaging*, *q-space imaging*

Chinese Library Classification No. R445; R742

Introduction

Multiple Sclerosis (MS) is a chronic inflammatory and neurodegenerative disease, characterized by widespread central nervous system damage that includes demyelinating white matter (WM) lesions and changes in normal-appearing white matter (NAWM) and gray matter. Conventional magnetic resonance imaging, including T2-weighted fluid-attenuated inversion recovery (T2-FLAIR) and pre- and post-contrast T1-weighted imaging, aids in establishing the diagnosis of MS and monitoring disease progression in a safe, noninvasive manner (Filippi and Rocca, 2007; Polman et al., 2011). These forms of conventional MRI, however, provide limited information regarding the underlying microstructural changes in MS. The mechanisms of the observed alterations in T2-FLAIR maps may be elucidated by diffusion magnetic resonance imaging (dMRI) approaches, which allow for probing human brain microstructure by measuring water diffusion properties influenced by the biologic activity of the surrounding tissues. Thus, advanced microstructural imaging biomarkers are potentially more sensitive to MS-specific microstructural changes than conventional T1- or T2-weighted imaging.

Among dMRI techniques, diffusion tensor imaging (DTI) is most widely used to study MS. DTI-derived parameters are well established to differ in patients with MS compared to controls (Filippi et al., 2000, 2001; Rovaris and Filippi, 2007; Warlop et al., 2009; Liu et al., 2012; Bester et al., 2013; Bodini et al., 2013; Harrison et al., 2013; Sbardella et al., 2013; Vishwas et al., 2013; Banaszek et al., 2015; Rocca et al., 2016; Schneider et al., 2017). DTI, however, has inherent limitations. First, DTI uses a simplified mono-Gaussian diffusion model that limits the technique to the approximation of a single fiber at each voxel; thus, DTI-derived indices may be biased in WM tracts that contain crossing fibers (Wheeler-Kingshott and Cercignani, 2009; Kodiweera et al., 2016). Second, DTI is a second-order approximation of the complex diffusion function that comprises a mixture of diffusion compartments.

The finer granularity of diffusion compartments can be assessed using higher-order diffusion modeling. Diffusion signals in WM tissue are modeled with different approaches: fast and slow diffusion components (Clark and Le Bihan, 2000); anisotropic hindered and restricted compartments (Jespersen et al., 2010; Fieremans et al., 2011; De Santis et al., 2013); fast isotropic free water and anisotropic tissue compartments (Pasternak et al., 2009); three compartments of fast isotropic diffusion, slow restricted isotropic diffusion, and restricted anisotropic diffusion (Chiang et al., 2014); and three compartments of fast isotropic diffusion (*e.g.*, CSF), anisotropic hindered diffusion (*e.g.*, extracellular water), and highly restricted anisotropic diffusion (*e.g.*, intra-axonal compartments) (Zhang et al., 2012). The output parameters from diffusion modeling are potentially less ambiguous than those of DTI for characterizing diffusion-weighted microstructures with increased specificity in clinical studies of the human brain.

Herein, we performed a feasibility study using one of the three-compartment models, neurite orientation dispersion and density imaging (NODDI). The NODDI axonal density index in WM was almost identical to the values obtained from electron microscopy of *ex vivo* mouse brain and is in good agreement with previously reported fiber densities of human brain using electron microscopy (Sepehrband et al., 2015); and the neurite density index in gray matter correlates with tau pathology in an animal model of Alzheimer's

disease (Colgan et al., 2015). The NODDI model was validated in *ex vivo* spinal cord with MS pathology in a study concluding that the NODDI-derived diffusion metrics match their histologic counterparts (Grussu et al., 2017). Other NODDI applications include *in vivo* human studies of MS (Schneider et al., 2017), classic galactosemia (Timmers et al., 2015), neonatal encephalopathy (Lally et al., 2014), WM development in the newborn (Kunz et al., 2014), brain aging (Billiet et al., 2015; Nazeri et al., 2015; Kodiweera et al., 2016), and mild traumatic brain injury (Mustafi et al., 2016), and has yielded valuable microstructural information on neurologic disorders of the human brain.

Alternatively, microstructural changes in WM may be studied by a non-parametric analysis, q-space imaging. The q-space approach estimates the water diffusion function, the probability density function (PDF), also called mean apparent propagator (MAP) (Ozarslan et al., 2013) or ensemble average propagator (EAP) (Descoteaux et al., 2011; Hosseinbor et al., 2013), through a Fourier transform relationship (Callaghan, 1991): $P(\vec{R}, \Delta) = FT^{-1}[E_\Delta(\vec{q})]$, where P is PDF; $\vec{R}$ is the displacement vector; Δ is the diffusion time; E is the normalized q-space signal; and $\vec{q}$ is the q-space wavevector determined by the diffusion gradient strength ($\vec{G}$) and the duration (δ), $\vec{q} = \gamma \vec{G} \delta$. The zero displacement probability, P_0, is the return to origin probability ($P_0 = P(\vec{R} = 0, \Delta)$), and represents the probability of those water molecules having no net diffusion within the diffusion time Δ. P_0 is often interpreted as a measure of restricted diffusion and cellularity (Assaf et al., 2000; Wu and Alexander, 2007; Ozarslan et al., 2013). In animal studies of dysmyelination, P_0 exhibited high sensitivity to myelination and brain maturation (Biton et al., 2006; Wu et al., 2011), consistent with other studies of P_0 in demyelination of the human brain with MS (Assaf et al., 2002, 2005). These studies show decreased P_0 associated with myelin-deficient WM and NAWM in MS.

In the present study, we used hybrid diffusion imaging (HYDI) (Wu and Alexander, 2007), a flexible and versatile dMRI technique, to acquire multishell diffusion data in patients with MS and clinically isolated syndrome (first episode of neurologic symptoms consistent with MS). The HYDI approach conveniently enables complementary data-processing strategies, such as model-fitting and non-parametric analyses, using one diffusion dataset. Here, the microstructural changes were characterized by the above-mentioned dMRI metrics in MS lesions, perilesion areas (hereafter referred to as perilesions), and NAWM. Statistical comparisons between types of tissues were performed for individual sets of regions of interest (ROIs) including a lesion, a matched perilesion, and NAWM (36 sets), and also at the group level.

Participants and Methods

Participants

Six female patients (age 52.8 ± 4.3 years), diagnosed and classified according to internationally accepted criteria (Kurtzke, 1983; Polman et al., 2011), participated in this observational study from Dartmouth-Hitchcock Medical Center ([Table 1](#)). Four had relapsing-remitting MS, one had secondary progressive MS, and one had clinically isolated syndrome. Neurologic disability level, measured using the Expanded Disability Status Scale (EDSS) (Kurtzke, 1983), was mild to moderate, with scores ranging from 1.5 to 3.5 (out of 10). All of the participants were at least 1 month post-exacerbation and post-steroid therapy, and had had no change in disease-modifying therapy within the preceding month. Patients with other neurologic disorders or a current substance use disorder were excluded from the study. All participants provided informed consent approved by the guidelines of the institutional review board of the Geisel School of Medicine at Dartmouth on October 17, 2013 (No. 11482) and all procedures were in accordance with an

institutional review board-approved study plan.

Image acquisition

Images were acquired using a Philips 3T Achieva scanner (Cleveland, OH, USA) with an 8-channel head coil. T1-weighted images were acquired using a 3D magnetization-prepared rapid gradient echo (MPRAGE) sequence with echo time (TE) = 3.3 ms, repetition time (TR) = 6.8 ms, field of view (FOV) = 240 mm, voxel size = $1.2 \times 1 \times 1$ mm, and 140 sagittal slices. Two-dimensional axial T2-FLAIR scans were obtained with: inversion time = 2800 ms, TE/TR = 125/11,000 ms, FOV = 240 mm, in-plane resolution of 0.94 mm, and 44 slices with a 3-mm slice thickness. The HYDI sequence used single-shot spin-echo echo-planar imaging (SS SE EPI) with five diffusion-weighting b-value shells (b = 250, 1000, 2250, 4000, and 6250 s/mm^2) and 143 diffusion-weighting gradient directions (**Table 2**). HYDI MR parameters were: TE/TR = 114.24/3590 ms, diffusion gradient duration (δ) = 46 ms and separation (Δ) = 58.4 ms, 2-mm in-plane resolution, 40 axial slices with 3-mm slice thickness, and a parallel imaging SENSE factor of 2. The total scan time for HYDI was 24 minutes.

HYDI data analyses

Pre-processing

All the diffusion data were visually inspected for severe scanner-related artifacts or motion artifacts prior to entering the pre-processing pipeline. The HYDI data pre-processing pipeline included denoising with a local principal component analysis approach (Manjon et al., 2013) and eddy current and motion corrections using the *eddy_correct* tool from the diffusion processing toolbox in the FMRIB Software Library (FSL) (https://fsl.fmrib.ox.ac.uk/fsl/fslwiki) (Jenkinson et al., 2002). All of the images, including T1-weighted and T2-FLAIR images, were transformed to the diffusion space where the b_0 image (i.e., the first image in HYDI with zero diffusion weighting) served as a common reference. Linear registration was performed to align the T1-weighted and T2-FLAIR images with the b_0 image using the FLIRT toolbox in FSL with seven parameters, including six rigid-body parameters and one global rescaling parameter. The same b_0 image was also used as the reference image in FSL *eddy_correct* for registering the remaining diffusion-weighted images.

DTI

DTI indices, including axial diffusivity (AD), radial diffusivity (RD), mean diffusivity (MD), and fractional anisotropy (FA), were computed using inner HYDI shells with b-values of 0, 250, and 1000 s/mm^2 (**Table 2**). The DTI analysis used the *dtifit* command in the FSL software package (Behrens et al., 2003). AD is the major eigenvalue of the diffusion tensor; RD is defined as the mean of the medium and minor eigenvalues of the diffusion tensor; MD is the mean of the three eigenvalues; and FA is the normalized variation of the three eigenvalues (Basser et al., 1994).

NODDI

NODDI metrics were computed with the whole HYDI dataset. The NODDI formalism describes the detectable normalized diffusion signal A = $V_{iso}A_{iso} + (1 - V_{iso})$ [$V_{ic}A_{ic} + V_{ec}A_{ec}$] (**Figure 1**), where V_{iso} and V_{ic} are the volume fractions of fast isotropic diffusion of CSF and intracellular water, respectively. The extracellular volume fraction is $V_{ec} = (1–V_{ic})$, a complementary value to V_{ic} (Zhang et al., 2012). The

symbols A_{iso}, A_{ic}, and A_{ec} represent the signal contributions from the fast isotropic diffusion (*e.g.*, CSF), intracellular (intra-axonal), and extracellular (extra-axonal) compartments, respectively. Using the Watson distribution, NODDI analysis also provides an estimate of the orientation dispersion index (ODI) describing an averaged dispersion of axons within an imaging voxel in WM. NODDI metrics were computed on a voxel-by-voxel basis with nonlinear fits coded in a MATLAB toolbox provided by the Microstructure Imaging Group at University College London (http://mig.cs.ucl.ac.uk/index.php?n=Tutorial.NODDIMATLAB). For NODDI fitting, the initial conditions for isotropic free-water diffusivity and the intrinsic diffusivity of the neural tissue were set to 3×10^{-3} mm^2/s and 1.7×10^{-3} mm^2/s, respectively, as suggested previously (Zhang et al., 2012).

q-Space analyses

P_0 was computed using the whole HYDI data set with a q-space analysis approach using in-house MATLAB code (Wu and Alexander, 2007; Wu et al., 2008). Table 3 summarizes the diffusion metrics' acronyms, units, intensity ranges, and microstructural implications.

ROI

A whole-brain WM mask was segmented using the FSL FAST toolbox on subject's co-registered T1-weighted MPRAGE images in the diffusion space (see *Pre-processing*). This WM mask may or may not contain lesions, which will eventually be excluded by the lesion masks described below. For each subject, within the WM, three ROI types were selected. Lesion (red in **Figure 2**): T2-FLAIR hyperintense lesions were segmented using an in-house semi-automated approach (Wishart et al., 2010). All segmented WM lesions were used in this study while gray matter lesions were excluded. Perilesion (blue in **Figure 2**): Perilesions were WM voxels that surrounded the lesions with a thickness of one voxel. Similar to (Colasanti et al., 2014), the perilesion WM voxels were generated by intersecting dilated lesion masks and the WM mask. NAWM (green in **Figure 2**): NAWM were WM voxels surrounding the perilesions, but with a gap of at least one voxel from the perilesion. Similarly, the NAWM ROIs were also generated using the dilation approach. As demonstrated in **Figure 2**, a set of ROIs includes a lesion (red), a matched perilesion (blue), and NAWM (green); in this case, there were six sets identified for Patient no. 4. All ROIs were three dimensional and extended across several slices depending on their sizes.

Statistical analyses

For each ROI, the means and standard deviations were computed for eight MRI measures: T2-FLAIR intensity and the seven diffusion metrics. Image data were assessed for outliers using boxplots and excluded if the values were outside the median $\pm$ 1.5 interquartile range (IQR). *At the individual lesion level*: For each set of ROIs, pairwise comparisons were performed between the lesion, matched perilesion, and NAWM, followed by multiple-comparison adjustment (across MRI measures and ROI sets). A false discovery rate (FDR) of less than 5% (*i.e.*, q-value < 0.05) was considered significant. For each MRI measure and each comparison pair, the number of significant ROI sets was summarized as a percentage relative to the total number of sets detected in the participants. *At the group level*: Means of each ROI were collected according to the type of ROI (*i.e.*, lesion, perilesion, and NAWM). The means of means and standard deviations of means were compared for each type of ROI by analysis of variance (ANOVA). Because T2-FLAIR intensity is not a quantitative measure, it was only included in the comparisons at the individual ROI level within individual subjects, and not in the group level analyses. Mauchly's test of sphericity (Mauchly, 1940) was calculated for each ANOVA, and when the test indicated a violation of sphericity, the Greenhouse-

Geisser adjustment was applied. Given the number of ANOVAs utilized in our analysis, we applied Bonferroni's adjustment for multiple comparisons, yielding a critical (P) threshold of 0.007 (0.05/7 diffusion indices). For ANOVAs with a significant overall result, additional *post hoc* pairwise testing comparing between the three ROI types (*i.e.*, lesion, perilesion, and NAWM) was conducted, with Bonferroni's adjustment applied for three pairwise comparisons with a critical $P = 0.017$ (0.05/3 pairs). All analyses were performed using IBM SPSS Statistics, version 23 (IBM, Armonk, NY, USA).

Results

Typical maps of AD, RD, MD, FA, ODI, V_{ic}, and P_0 from a group of healthy volunteers (not included in this study) are shown in **Additional Figure 1**. Similar maps for two patients from this study are shown in **Figure 3**. As expected from the parameter descriptions in **Table 3**, AD and RD have high WM contrast only in compact fiber tracts with known single fiber bundles, such as the anterior and posterior limbs of the internal capsule and corpus callosum. MD in the ventricles is very high, approximately 3×10^{-3} mm^2/s. This value is close to the isotropic free diffusivity value in the cerebrospinal fluid as assumed in the NODDI calculations. FA maps show high intensity (> 0.5) in the WM, indicating high tissue coherence, and low intensity in grey matter (< 0.2) and cerebrospinal fluid, indicating more isotropic diffusion. Consistently, WM has a lower intensity (< 0.3) in the ODI maps, indicating lower dispersion (*i.e.*, high coherence). Typical WM also has high intensity in the V_{ic} map (> 0.7), which represents axonal density under the rigid stick assumption. The P_0 map shows higher intensity in areas with restricted diffusion (*e.g.*, WM and deep brain gray matter) and intensity > 0.8, as expected. Hyperintense lesions can be appreciated in the T2-FLAIR maps (**Figure 3**), whereas corresponding hypointense areas are observed in the FA, V_{ic}, and P_0 maps.

Additional Figure 1

Averaged AD, RD, MD, FA, ODI, V_{ic}, and P_0 maps from a group of healthy volunteers (not included in this study).

The gray scale for AD, RD, and MD ranges from 0 to 3.0 x10^{-3} mm^2/s. The gray scale for FA is from 0.2 to 1; the larger the value, the higher the tissue coherence. The gray scale of the ODI map is from 0 to 1, while that of V_{ic} is from 0.1 to 1. A smaller ODI indicates higher coherence and less dispersion, while a larger V_{ic} indicates higher intra-cellular volume fraction. AD: Axial diffusivity; RD: radial diffusivity; MD: mean diffusivity; FA: fractional anisotropy; ODI: orientation dispersion index; V_{ic}: volume fraction for intra-axonal water; P_0: q-space derived zero-displacement probability.

Thirty-six lesions were segmented by an intensity-based semi-automated approach on T2-FLAIR images (Wishart et al., 2010). Thus, there were 36 sets of ROIs for lesions, perilesions, and NAWM. Table 4 lists the patient number, set number, ROI size, and their anatomic locations in the WM.

At the individual lesion level

No outliers were evident in the image data. Results (q-values) of the pairwise comparisons between the lesion, matched perilesion, and NAWM are listed in **Additional Table 1**, whereas Table 5 summarizes the

percentage of significant sets for each MRI measure and comparison pair. Most of the MRI measures demonstrated significant differences between lesions and the other two ROIs (*i.e.*, perilesions and NAWM) in more than 80% of the ROI sets, except ODI, which did not differ between the three types of ROIs. For comparisons between perilesions and NAWM, only V_{ic} and P_0 were significantly different at least 89% of the ROI sets.

> **Additional Table 1**
>
> Results (q-values) of the pairwise comparisons between the lesion, matched perilesion, and NAWM

At the group level

The means and standard deviations for each MRI measure and ROI type are listed in **Table 6**. The table also lists the results of the ANOVAs and *post-hoc* pairwise *t*-tests. None of the DTI indices (AD, RD, MD, and FA) and NODDI-derived ODI differed significantly between ROIs. V_{ic} and P_0 differed among the three ROIs with a corrected $P < 0.007$. *Post-hoc* testing showed that V_{ic} and P_0 were significantly decreased (corrected $P < 0.017$) in lesions and perilesions compared with NAWM. The bar plots of the diffusion metrics in the three ROI types with significant findings are shown in **Figure 4** with overhead arrows representing significant pairwise *t*-tests. T2-FLAIR intensity and DTI indices were similar between perilesions and NAWM, whereas V_{ic} and P_0 differed significantly in these two ROIs. Further, the extent of changes in the perilesions was intermediate between that in the lesions and NAWM.

Discussion

In this study, a flexible dMRI technique, HYDI, was used to investigate changes in microstructural indices derived from different modeling approaches. The HYDI method is versatile and conducive to multiple strategies of diffusion data processing (Wu and Alexander, 2007; Wu et al., 2008). HYDI has at least 126 diffusion directions, which requires approximately 25 minutes of scan time with parallel imaging and less than 7 minutes when using simultaneous multislice (also called multi-band) techniques (Setsompop et al., 2012).

Using the HYDI dataset, we studied the differences in DTI indices (AD, RD, MD, and FA), NODDI indices (ODI and V_{ic}), and P_0 across lesion, perilesion, and NAWM ROIs in patients with MS. Compared with NAWM, MS lesions were characterized by decreased tissue restriction as described by P_0, a model-free index from q-space analysis. Consistent with previous studies in an animal model of MS (Biton et al., 2006; Wu et al., 2011), decreased P_0 suggests the deterioration of myelination and/or the absence of myelinated axons. The loss of myelinated axons is further implied by a decreased in V_{ic}, a NODDI index of axonal density, consistent with an *ex vivo* MS spinal cord study (Grussu et al., 2017).

At both the lesion level and group level, V_{ic} and P_0 detected WM alterations between the perilesions and NAWM that were not detected in T2-FLAIR. Alterations of WM in these perilesion ROIs were significant, though more subtle than those in the lesions. Similarly, previous studies, though with different imaging modalities, demonstrated that MS perilesions are moderately associated with a decreased intensity of the magnetization transfer ratio, increased microglial density (Moll et al., 2011), and increased binding with a PET inflammation tracer, 18-kDa translocator protein (Colasanti et al., 2014). Our preliminary results suggest that dMRI metrics are sensitive to subtle changes in MS-affected WM that are not detectable using

conventional imaging approaches. An advantage of model based diffusion metrics and q-space analysis is that they can provide insights into the underlying mechanisms.

In this study, the fiber dispersion inferred based on NODDI-derived ODI did not differ significantly among the three ROI types (*i.e.*, lesions, perilesions, and NAWM). While not seen in the group level tests due to variations across ROI sets, decreased FA was observed at the individual lesion level and is consistent with a decrease in tissue coherence, as seen in previous reports of adult mild MS (Filippi et al., 2000), adult moderate MS (Filippi et al., 2001), and pediatric mild MS (Vishwas et al., 2013; Rocca et al., 2016). DTI diffusivities (*i.e.*, AD, RD, and MD) have discrimination capabilities comparable to T2-FLAIR in separating the lesions from the rest of the WM. In this study they failed to distinguish perilesions from NAWM. The potential explanation may be the stringent multiple comparison adjustment filtered out those DTI metrics, which were otherwise significant.

This feasibility study has several limitations. First, although there were 36 ROIs, they were obtained from only six subjects, which could undermine the DTI results. In addition, the differences in subjects' disease stage, ROI size, and anatomical locations of ROIs with distinct underlying microstructural compositions may contribute additional variations in the results. It is also possible that different anatomical locations of ROIs may have different degrees or types of neurodegeneration. Future studies may focus on the implication of anatomically varying diffusion metrics to underlying pathophysiological changes in MS.

Second, NODDI may not be the best model for characterizing MS lesions. While NODDI-derived V_{ic} for axonal density is robust within WM, it tends to be overestimated in tissues with intermediate to low microscopic anisotropy, such as gray matter and lesions (Jelescu et al., 2016; Lampinen et al., 2017). The overestimation of NODDI could be caused by a violation of the NODDI assumptions of tortuosity and "rigid-stick" describing fixed axial diffusivities and close to zero radial diffusivity (compared with axial diffusivity). Further investigation is necessary to estimate intra-axonal diffusivities through other diffusion models, such as diffusion kurtosis imaging (Fieremans et al., 2011), diffusion basis spectrum imaging (Wang et al., 2011), restriction spectrum imaging (White et al., 2013), or the constrained diffusional variance decomposition method (Lampinen et al., 2017).

Finally, the definition of lesion, perilesion and NAWM ROIs may affect the results. In this study, lesion ROIs were defined based on a procedure optimized for detection of T2-FLAIR hyperintense regions. In addition, a small percentage (approximately 1.37 lesion count per brain (Wen et al., 2009)) of the lesions may be age-related white matter hyperintensities. It is also possible that perilesions have a partial volume effect from NAWM. Despite these factors, this study provides evidence and novel insights regarding the microstructural alterations from NAWM to intermediate perilesion areas to MS lesions.

Additional files:

Additional Figure 1: *Averaged AD, RD, MD, FA, ODI, Vic, and P0 maps from a group of healthy volunteers.*

Additional Table 1: *Results (q-values) of the pairwise comparisons between the lesion, matched perilesion, and NAWM.*

Footnotes

Conflicts of interest: *No competing financial interests exist.*

References

1. Assaf Y, Mayk A, Cohen Y. Displacement imaging of spinal cord using q-space diffusion-weighted MRI. Magn Reson Med. 2000;44:713–722. [PubMed: 11064406]

2. Assaf Y, Chapman J, Ben-Bashat D, Hendler T, Segev Y, Korczyn AD, Graif M, Cohen Y. White matter changes in multiple sclerosis: correlation of q-space diffusion MRI and 1H MRS. Magn Reson Imaging. 2005;23:703–710. [PubMed: 16198825]

3. Assaf Y, Ben-Bashat D, Chapman J, Peled S, Biton IE, Kafri M, Segev Y, Hendler T, Korczyn AD, Graif M, Cohen Y. High b-value q-space analyzed diffusion-weighted MRI: application to multiple sclerosis. Magn Reson Med. 2002;47:115–126. [PubMed: 11754450]

4. Banaszek A, Bladowska J, Pokryszko-Dragan A, Podemski R, Sasiadek MJ. Evaluation of the

degradation of the selected projectile, commissural and association white matter tracts within normal appearing white matter in patients with multiple sclerosis using diffusion tensor MR imaging - a preliminary study. Pol J Radiol. 2015;80:457–463. [PMCID: PMC4603607] [PubMed: 26516389]

5. Basser PJ, Mattiello J, LeBihan D. MR diffusion tensor spectroscopy and imaging. Biophys J. 1994;66:259–267. [PMCID: PMC1275686] [PubMed: 8130344]

6. Behrens TE, Woolrich MW, Jenkinson M, Johansen-Berg H, Nunes RG, Clare S, Matthews PM, Brady JM, Smith SM. Characterization and propagation of uncertainty in diffusion-weighted MR imaging. Magn Reson Med. 2003;50:1077–1088. [PubMed: 14587019]

7. Bester M, Lazar M, Petracca M, Babb JS, Herbert J, Grossman RI, Inglese M. Tract-specific white matter correlates of fatigue and cognitive impairment in benign multiple sclerosis. J Neurol Sci. 2013;330:61–66. [PMCID: PMC4651179] [PubMed: 23643443]

8. Billiet T, Vandenbulcke M, Madler B, Peeters R, Dhollander T, Zhang H, Deprez S, Van den Bergh BR, Sunaert S, Emsell L. Age-related microstructural differences quantified using myelin water imaging and advanced diffusion MRI. Neurobiol Aging. 2015;36:2107–2121. [PubMed: 25840837]

9. Biton IE, Duncan ID, Cohen Y. High b-value q-space diffusion MRI in myelin-deficient rat spinal cords. Magn Reson Imaging. 2006;24:161–166. [PubMed: 16455404]

10. Bodini B, Cercignani M, Khaleeli Z, Miller DH, Ron M, Penny S, Thompson AJ, Ciccarelli O. Corpus callosum damage predicts disability progression and cognitive dysfunction in primary-progressive MS after five years. Hum Brain Mapp. 2013;34:1163–1172. [PubMed: 22328451]

11. Callaghan PT. Principles of nuclear magnetic resonance microscopy. Oxford: Clarendon Press; 1991.

12. Chiang CW, Wang Y, Sun P, Lin TH, Trinkaus K, Cross AH, Song SK. Quantifying white matter tract diffusion parameters in the presence of increased extra-fiber cellularity and vasogenic edema. Neuroimage. 2014;101:310–319. [PMCID: PMC4165711] [PubMed: 25017446]

13. Clark CA, Le Bihan D. Water diffusion compartmentation and anisotropy at high b values in the human brain. Magn Reson Med. 2000;44:852–859. [PubMed: 11108621]

14. Colasanti A, Guo Q, Muhlert N, Giannetti P, Onega M, Newbould RD, Ciccarelli O, Rison S, Thomas C, Nicholas R, Muraro PA, Malik O, Owen DR, Piccini P, Gunn RN, Rabiner EA, Matthews PM. *In vivo* assessment of brain white matter inflammation in multiple sclerosis with (18)F-PBR111 PET. J Nucl Med. 2014;55:1112–1118. [PubMed: 24904112]

15. Colgan N, Siow B, O'Callaghan JM, Harrison IF, Wells JA, Holmes HE, Ismail O, Richardson S, Alexander DC, Collins EC, Fisher EM, Johnson R, Schwarz AJ, Ahmed Z, O'Neill MJ, Murray TK, Zhang H, Lythgoe MF. Application of neurite orientation dispersion and density imaging (NODDI) to a tau pathology model of Alzheimer's disease. Neuroimage. 2015;125:739–744. [PMCID: PMC4692518] [PubMed: 26505297]

16. De Santis S, Drakesmith M, Bells S, Assaf Y, Jones DK. Why diffusion tensor MRI does well only some of the time: Variance and covariance of white matter tissue microstructure attributes in the living human brain. Neuroimage. 2013;89:35–44. [PMCID: PMC3988851] [PubMed: 24342225]

17. Descoteaux M, Deriche R, Le Bihan D, Mangin JF, Poupon C. Multiple q-shell diffusion propagator

imaging. Med Image Anal. 2011;15:603–621. [PubMed: 20685153]

18. Fieremans E, Jensen JH, Helpern JA. White matter characterization with diffusional kurtosis imaging. Neuroimage. 2011;58:177–188. [PMCID: PMC3136876] [PubMed: 21699989]

19. Filippi M, Rocca MA. Conventional MRI in multiple sclerosis. J Neuroimaging. 2007;17(Suppl 1):3S–9S. [PubMed: 17425727]

20. Filippi M, Cercignani M, Inglese M, Horsfield MA, Comi G. Diffusion tensor magnetic resonance imaging in multiple sclerosis. Neurology. 2001;56:304–311. [PubMed: 11171893]

21. Filippi M, Iannucci G, Cercignani M, Assunta Rocca M, Pratesi A, Comi G. A quantitative study of water diffusion in multiple sclerosis lesions and normal-appearing white matter using echo-planar imaging. Arch Neurol. 2000;57:1017–1021. [PubMed: 10891984]

22. Grussu F, Schneider T, Tur C, Yates RL, Tachrount M, Ianus A, Yiannakas MC, Newcombe J, Zhang H, Alexander DC, DeLuca GC Gandini Wheeler-Kingshott CAM. Neurite dispersion: a new marker of multiple sclerosis spinal cord pathology? Ann Clin Transl Neurol. 2017;4:663–679. [PMCID: PMC5590517] [PubMed: 28904988]

23. Harrison DM, Shiee N, Bazin PL, Newsome SD, Ratchford JN, Pham D, Calabresi PA, Reich DS. Tract-specific quantitative MRI better correlates with disability than conventional MRI in multiple sclerosis. J Neurol. 2013;260:397–406. [PMCID: PMC3753185] [PubMed: 22886062]

24. Hosseinbor AP, Chung MK, Wu YC, Alexander AL. Bessel Fourier Orientation Reconstruction (BFOR): an analytical diffusion propagator reconstruction for hybrid diffusion imaging and computation of q-space indices. Neuroimage. 2013;64:650–670. [PMCID: PMC3508305] [PubMed: 22963853]

25. Jelescu IO, Veraart J, Fieremans E, Novikov DS. Degeneracy in model parameter estimation for multi-compartmental diffusion in neuronal tissue. NMR Biomed. 2016;29:33–47. [PMCID: PMC4920129] [PubMed: 26615981]

26. Jenkinson M, Bannister P, Brady M, Smith S. Improved optimization for the robust and accurate linear registration and motion correction of brain images. Neuroimage. 2002;17:825–841. [PubMed: 12377157]

27. Jespersen SN, Bjarkam CR, Nyengaard JR, Chakravarty MM, Hansen B, Vosegaard T, Ostergaard L, Yablonskiy D, Nielsen NC, Vestergaard-Poulsen P. Neurite density from magnetic resonance diffusion measurements at ultrahigh field: comparison with light microscopy and electron microscopy. Neuroimage. 2010;49:205–216. [PMCID: PMC2862296] [PubMed: 19732836]

28. Kodiweera C, Alexander AL, Harezlak J, McAllister TW, Wu YC. Age effects and sex differences in human brain white matter of young to middle-aged adults: A DTI, NODDI, and q-space study. Neuroimage. 2016;128:180–192. [PMCID: PMC4824064] [PubMed: 26724777]

29. Kunz N, Zhang H, Vasung L, O'Brien KR, Assaf Y, Lazeyras F, Alexander DC, Huppi PS. Assessing white matter microstructure of the newborn with multi-shell diffusion MRI and biophysical compartment models. Neuroimage. 2014;96:288–299. [PubMed: 24680870]

30. Kurtzke JF. Rating neurologic impairment in multiple sclerosis: an expanded disability status scale (EDSS) Neurology. 1983;33:1444–1452. [PubMed: 6685237]

31. Lally P, Zhang H, Pauliah S, Price D, Bainbridge A, Balraj G, Cady E, Shankaran S, Thayyil S.

Microstructural changes in neonatal encephalopathy revealed with the neurite orientation dispersion and density imaging (NODDI) model. Arch Dis Child Fetal Neonatal Ed. 2014;99(Suppl 1):A14.

32. Lampinen B, Szczepankiewicz F, Martensson J, van Westen D, Sundgren PC, Nilsson M. Neurite density imaging versus imaging of microscopic anisotropy in diffusion MRI: A model comparison using spherical tensor encoding. Neuroimage. 2017;147:517–531. [PubMed: 27903438]

33. Liu Y, Mitchell PJ, Kilpatrick TJ, Stein MS, Harrison LC, Baker J, Ditchfield M, Li K, Egan GF, Butzkueven H, Kolbe SC. Diffusion tensor imaging of acute inflammatory lesion evolution in multiple sclerosis. J Clin Neurosci. 2012;19:1689–1694. [PubMed: 23084347]

34. Manjon JV, Coupe P, Concha L, Buades A, Collins DL, Robles M. Diffusion weighted image denoising using overcomplete local PCA. PLoS One. 2013;8:e73021. [PMCID: PMC3760829] [PubMed: 24019889]

35. Mauchly JW. Significance test for sphericity of a normal n-variate distribution. Ann Math Statist. 1940;11:204–209.

36. Moll NM, Rietsch AM, Thomas S, Ransohoff AJ, Lee JC, Fox R, Chang A, Ransohoff RM, Fisher E. Multiple sclerosis normal-appearing white matter: pathology-imaging correlations. Ann Neurol. 2011;70:764–773. [PMCID: PMC3241216] [PubMed: 22162059]

37. Mustafi SM, Kodiweera C, Flashman LA, McAllister TW, Wu YC. International Society of Magnetic Resonance in Medicine (ISMRM) 24th Annual Meeting. Singapore: 2016. Hybrid diffusion imaging to detect acute white matter injury after mild TBI.

38. Nazeri A, Chakravarty MM, Rotenberg DJ, Rajji TK, Rathi Y, Michailovich OV, Voineskos AN. Functional consequences of neurite orientation dispersion and density in humans across the adult lifespan. J Neurosci. 2015;35:1753–1762. [PMCID: PMC4308611] [PubMed: 25632148]

39. Ozarslan E, Koay CG, Shepherd TM, Komlosh ME, Irfanoglu MO, Pierpaoli C, Basser PJ. Mean apparent propagator (MAP) MRI: a novel diffusion imaging method for mapping tissue microstructure. Neuroimage. 2013;78:16–32. [PMCID: PMC4059870] [PubMed: 23587694]

40. Pasternak O, Sochen N, Gur Y, Intrator N, Assaf Y. Free water elimination and mapping from diffusion MRI. Magn Reson Med. 2009;62:717–730. [PubMed: 19623619]

41. Polman CH, Reingold SC, Banwell B, Clanet M, Cohen JA, Filippi M, Fujihara K, Havrdova E, Hutchinson M, Kappos L, Lublin FD, Montalban X, O'Connor P, Sandberg-Wollheim M, Thompson AJ, Waubant E, Weinshenker B, Wolinsky JS. Diagnostic criteria for multiple sclerosis: 2010 revisions to the McDonald criteria. Ann Neurol. 2011;69:292–302. [PMCID: PMC3084507] [PubMed: 21387374]

42. Rocca MA, Sonkin M, Copetti M, Pagani E, Arnold DL, Narayanan S, Sled JG, Banwell B, Filippi M. Diffusion tensor magnetic resonance imaging in very early onset pediatric multiple sclerosis. Mult Scler. 2016;22:620–627. [PubMed: 26199355]

43. Rovaris M, Filippi M. Diffusion tensor MRI in multiple sclerosis. J Neuroimaging. 2007;17(Suppl 1):27S–30S. [PubMed: 17425731]

44. Sbardella E, Tona F, Petsas N, Pantano P. DTI measurements in multiple sclerosis: Evaluation of brain damage and clinical implications. Mult Scler Int 2013. 2013:671730. [PMCID: PMC3628664] [PubMed: 23606965]

45. Schneider T, Brownlee W, Zhang H, Ciccarelli O, Miller DH, Wheeler-Kingshott CG. Sensitivity of multi-shell NODDI to multiple sclerosis white matter changes: a pilot study. Funct Neurol. 2017;32:97–101. [PMCID: PMC5507159] [PubMed: 28676143]

46. Sepehrband F, Clark KA, Ullmann JF, Kurniawan ND, Leanage G, Reutens DC, Yang Z. Brain tissue compartment density estimated using diffusion-weighted MRI yields tissue parameters consistent with histology. Hum Brain Mapp. 2015;36:3687–3702. [PMCID: PMC4545675] [PubMed: 26096639]

47. Setsompop K, Gagoski BA, Polimeni JR, Witzel T, Wedeen VJ, Wald LL. Blipped-controlled aliasing in parallel imaging for simultaneous multislice echo planar imaging with reduced g-factor penalty. Magn Reson Med. 2012;67:1210–1224. [PMCID: PMC3323676] [PubMed: 21858868]

48. Timmers I, Zhang H, Bastiani M, Jansma BM, Roebroeck A, Rubio-Gozalbo ME. White matter microstructure pathology in classic galactosemia revealed by neurite orientation dispersion and density imaging. J Inherit Metab Dis. 2015;38:295–304. [PMCID: PMC4341012] [PubMed: 25344151]

49. Vishwas MS, Healy BC, Pienaar R, Gorman MP, Grant PE, Chitnis T. Diffusion tensor analysis of pediatric multiple sclerosis and clinically isolated syndromes. AJNR Am J Neuroradiol. 2013;34:417–423. [PubMed: 22859275]

50. Wang Y, Wang Q, Haldar JP, Yeh FC, Xie M, Sun P, Tu TW, Trinkaus K, Klein RS, Cross AH, Song SK. Quantification of increased cellularity during inflammatory demyelination. Brain. 2011;134:3590–3601. [PMCID: PMC3235568] [PubMed: 22171354]

51. Warlop NP, Achten E, Fieremans E, Debruyne J, Vingerhoets G. Transverse diffusivity of cerebral parenchyma predicts visual tracking performance in relapsing-remitting multiple sclerosis. Brain Cogn. 2009;71:410–415. [PubMed: 19576672]

52. Wen W, Sachdev PS, Li JJ, Chen X, Anstey KJ. White matter hyperintensities in the forties: their prevalence and topography in an epidemiological sample aged 44-48. Hum Brain Mapp. 2009;30:1155–1167. [PubMed: 18465744]

53. Wheeler-Kingshott CA, Cercignani M. About "axial" and "radial" diffusivities. Magn Reson Med. 2009;61:1255–1260. [PubMed: 19253405]

54. White NS, Leergaard TB, D'Arceuil H, Bjaalie JG, Dale AM. Probing tissue microstructure with restriction spectrum imaging: Histological and theoretical validation. Hum Brain Mapp. 2013;34:327–346. [PMCID: PMC3538903] [PubMed: 23169482]

55. Wishart HA, Kee ER, Ford JF, MacDonald JW, Aney S, J. LZ. Acapulco, Mexico: Annual Meeting of the International Neuropsychological Society; 2010. A novel approach for semi-automated segmentation of MS lesions on FLAIR imaging: Reliability and clinical correlates.

56. Wu YC, Alexander AL. Hybrid diffusion imaging. Neuroimage. 2007;36:617–629. [PMCID: PMC2428345] [PubMed: 17481920]

57. Wu YC, Field AS, Alexander AL. Computation of diffusion function measures in q-space using magnetic resonance hybrid diffusion imaging. IEEE Trans Med Imaging. 2008;27:858–865. [PMCID: PMC2674390] [PubMed: 18541492]

58. Wu YC, Field AS, Duncan ID, Samsonov AA, Kondo Y, Tudorascu D, Alexander AL. High b-value

and diffusion tensor imaging in a canine model of dysmyelination and brain maturation. Neuroimage. 2011;58:829–837. [PMCID: PMC3166414] [PubMed: 21777681]

59. Zhang H, Schneider T, Wheeler-Kingshott CA, Alexander DC. NODDI: practical *in vivo* neurite orientation dispersion and density imaging of the human brain. Neuroimage. 2012;61:1000–1016. [PubMed: 22484410]

Figures and Tables

Table 1

Demographics and characteristics of all the included patients

	Mean	SD	Range
Age (year)	52.8	4.3	45 – 58
Disease duration (year)	8.8	7.0	1 – 20
EDSS	2.6	0.8	1.5 – 3.5

EDSS: Expanded Disability Status Scale; SD: standard deviation.

Table 2

Hybrid diffusion imaging (HYDI) encoding scheme

HYDI shell	Ne	b-value (s/mm^2)
0	1	0
1st	6	250
2nd	21	1000
3rd	24	2250
4th	30	4000
5th	61	6250
Total	143	

Ne: Number of encoding directions.

Figure 1
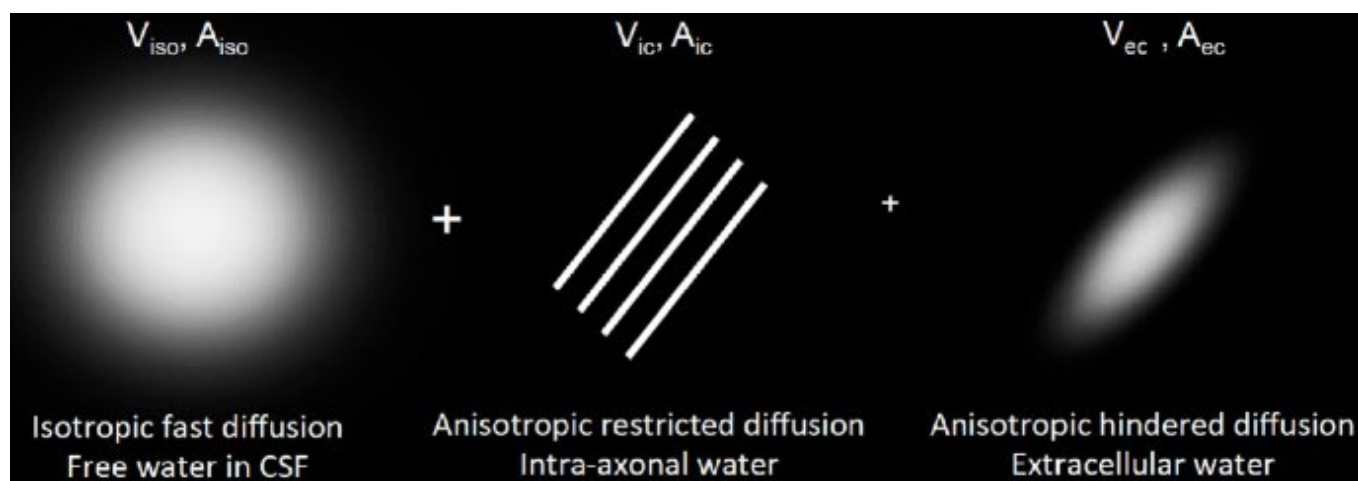
Visualization of diffusion compartments in the NODDI model.

V_{iso} and V_{ic} are the volume fraction of the free isotropic diffusion and intra-axonal compartment, respectively. The extracellular volume fraction is $V_{ec} = (1 - V_{ic})$, a complement number to V_{ic}. A_{iso}, A_{ic}, and A_{ec} are the normalized diffusion signal contributed from individual diffusion compartments. A_{ec}: Diffusion signal from extra-axonal water; A_{ic}: diffusion signal from intra-axonal water; A_{iso}: diffusion signal from isotropic fast diffusion; NODDI: neurite orientation dispersion and density imaging; V_{ec}: volume fraction for extra-cellular water; V_{ic}: volume fraction for intra-axonal water; V_{iso}: volume fraction for isotropic fast diffusion; CSF: cerebrospinal fluid.

Table 3

Abbreviations of diffusion metrics

Model	Diffusion indices	Unit	Intensity range	Microstructural implications and comments
DTI	AD	10^{-3} mm²/s	0–3	Axial diffusivity; influenced by axonal damage, cell infiltration, and CSF contamination.
	RD	10^{-3} mm²/s	0–3	Radial diffusivity; influenced by myelination, inflammation, acute axonal damage, and CSF contamination.
	MD	10^{-3} mm²/s	0–3	Averaged diffusivity across diffusion compartments
	FA	AU	0–1	WM coherence; influenced by both fiber coherence and fiber volume fraction.
NODDI	ODI	AU	0–1	WM fiber dispersion with stick assumption for fiber and Watson distribution.
	V_{ic}	AU	0–1	Volume fraction of intracellular compartment, also axonal density under stick model assumption in the tissue parenchyma, i.e., $(V_{ic} + V_{ec}) = (1 - V_{iso})$.
	V_{ec}	AU	0–1	Volume fraction of extracellular compartment in the tissue parenchyma, $V_{ec} = 1 - V_{ic}$
	V_{iso}	AU	0–1	Volume fraction of the fast diffusion compartment; influenced by CSF contamination and parenchymal atrophy.
q-space	P_0	AU	0–1	Probability of water molecules that had minimal diffusion within a given diffusion time; insensitive to fiber orientations or crossing fibers; influenced by overall tissue restriction and cellularity.

DTI: Diffusion tensor imaging; NODDI: neurite orientation dispersion and density imaging; AD: axial diffusivity; RD: radial diffusivity; MD: mean diffusivity; FA: fractional anisotropy; ODI: orientation dispersion index; V_{ic}: intra-axonal volume fraction; V_{ec}: volume fraction for extra-cellular water; V_{iso}: volume fraction for isotropic fast diffusion; P_0: q-space derived zero-displacement probability; AU: arbitrary unit; CSF: cerebrospinal fluid.

Figure 2
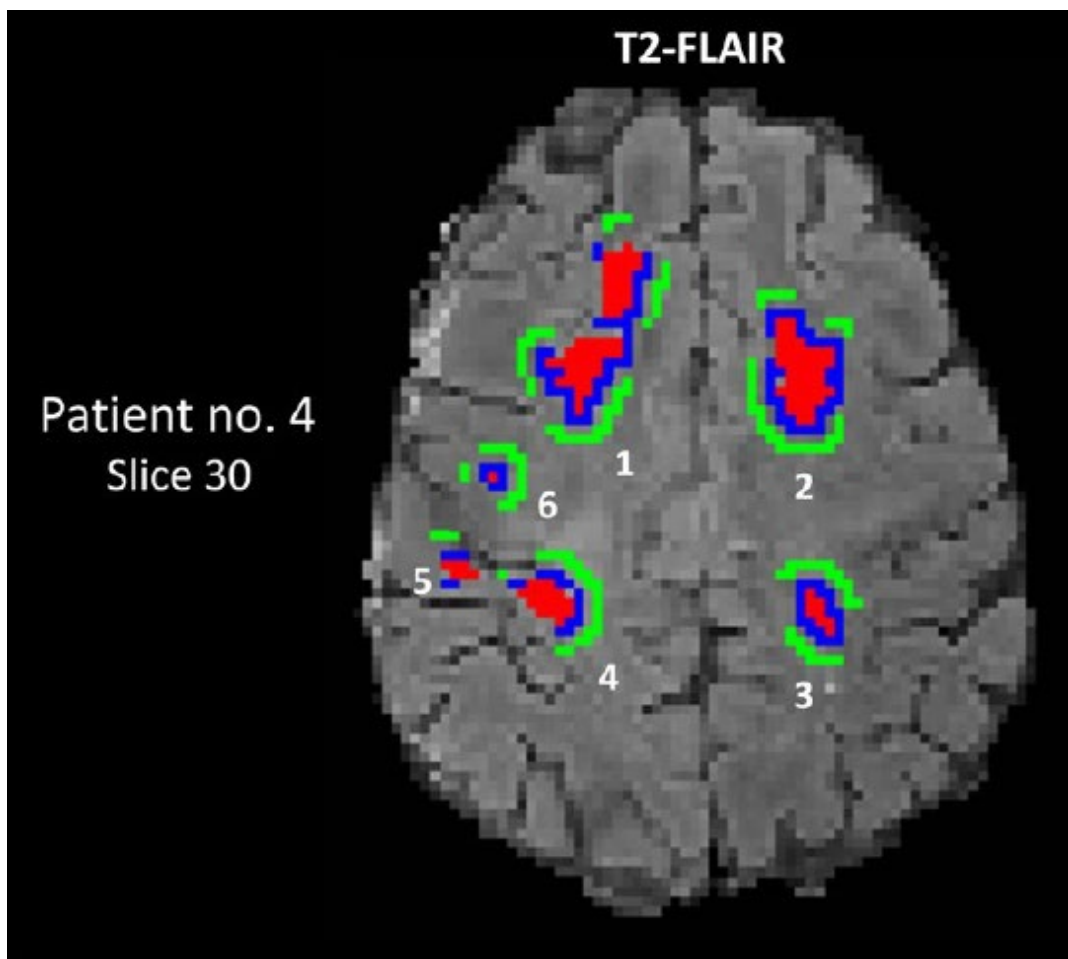
Segmentation of lesions, perilesions, and normal-appearing white matter (NAWM) on a T2-FLAIR map of patient No. 4.

A set of ROIs includes a lesion (red), a matched perilesion (blue) and NAWM (green); this patient (Expanded Disability Status Scale score was 3.5) had six sets of lesions (No. 4). The set number for this patient, sizes of corresponding ROIs, and anatomic locations in the white matter are listed in Table 4. The gray scale is 0–300 AU for the T2-FLAIR map. Numbers 1–6 denote ROI sets listed in Table 3. AU: Arbitrary unit; FLAIR: fluid attenuated inversion recovery; no: number; ROIs: regions of interest.

Figure 3
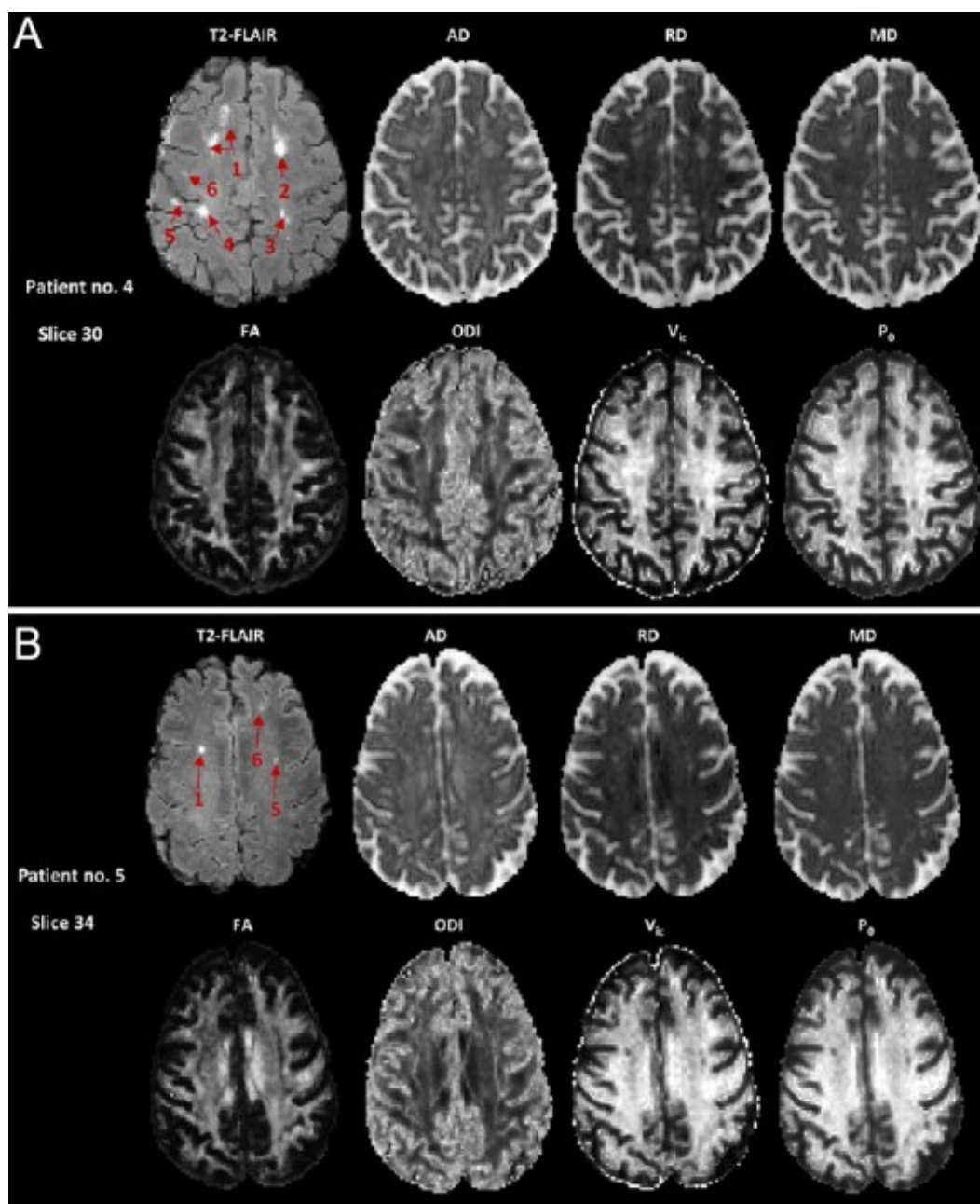
Co-registered MRI maps of two patients with multiple sclerosis (MS).

(A) Patient No. 4. Six hyperintense lesions in the T2-FLAIR image can be appreciated. Note that the two separated hyperintense regions of lesion 1 were connected in another slice (not shown). The lesion segmentation results in the same patient are shown in Figure 2. The corresponding areas in the diffusion maps appeared hyperintense in the AD, RD, and MD maps, and hypointense in the FA, V_{ic}, and P_0 maps. The gray scale is 0–300 AU for T2-FLAIR; $0–3 \times 10^{-3}$ mm^2/s for AD, RD, and MD; and 0–1 for FA, ODI, V_{ic}, and P_0. (B) Patient No. 5. Three hyperintense lesions in the T2-FLAIR image can be appreciated. AD: Axial diffusivity; AU: arbitrary unit; FA: fractional anisotropy; FLAIR: fluid attenuated inversion recovery; MD: mean diffusivity; ODI: orientation dispersion index; P_0: q-space derived zero-displacement probability; RD: radial diffusivity; V_{ic}: volume fraction for intra-axonal water.

Table 4

Classifications of region of interest (ROI)

| Patient number | Set number | Size (voxel) | | | Anatomic location[a] |
		Lesion	Perilesion	NAWM	
1	1	202	345	567	Genu of the corpus callosum
	2	103	267	345	Body of the corpus callosum
	3	35	78	58	Anterior limb of the internal capsule - Right
	4	28	53	42	Posterior limb of the internal capsule - Left
	5	18	28	35	Frontal pole
	6	12	34	38	Inferior temporal gyrus - Anterior
2	1	128	232	324	Anterior corona radiata - Right
	2	112	128	238	Superior corona radiata - Left
	3	78	82	156	Posterior corona radiata - Left
	4	56	89	168	Superior parietal lobule - Left
	5	42	93	132	Frontal medial - Right
	6	28	75	134	Subcallosal - Left
3	1	256	345	456	Cerebral peduncle - Right
	2	128	234	354	Superior longitudinal fasciculus - Left
	3	93	128	256	Superior longitudinal fasciculus - Right
	4	74	125	287	Cingulum gyrus (cingulate) - Right
	5	54	74	75	Occipital fusiform gyrus - Right
	6	36	45	52	Frontal orbital - Right
4	1	2983	1643	1468	Anterior limb of the internal capsule - Left
	2	858	310	717	Anterior limb of the internal capsule - Right
	3	301	310	452	Retro lenticular part of the internal capsule - Right
	4	52	47	47	Temporal occipital fusiform gyrus - Right
	5	22	27	25	Intracalcarine – Right
	6	15	28	28	Occipital fusiform gyrus - Right
5	1	354	421	452	Superior corona radiata - Left
	2	149	234	213	Body of the corpus callosum
	3	102	212	213	Cerebral peduncle - Right
	4	94	126	128	Fornix body
	5	53	102	98	Insular - Left
	6	24	56	57	Angular gyrus - Left
6	1	3223	2048	1788	Retro lenticular part of the internal capsule - Left
	2	788	1023	1233	Posterior thalamic radiation - Right
	3	345	565	457	Corticospinal tract - Right
	4	125	256	325	Cingulum gyrus (hippocampus) - Left
	5	78	121	134	Occipital pole
	6	65	98	101	Supracalcarine - Right

[a]All the ROIs were located in white matter or in the corresponding subcortical white matter. Johns Hopkins University white matter atlas and the Harvard cortical atlas provided in FMRIB software library were used to identify the anatomic locations *via* overlapping atlas and ROI masks. NAWM: Normal-appearing white matter; ROI: region of interest.

Table 5

Pairwise comparisons of diffusion parameters between lesion-perilesion, lesion-NAWM, and perilesion-NAWM at the level of individual set of ROIs

	Percentage (%) of significant ROI sets[a]		
MRI Measures	Lesion-perilesion	Lesion-NAWM	Perilesion-NAWM
T2-FLAIR	100	100	0
AD	94	94	3
RD	100	100	31
MD	100	100	31
FA	81	83	19
ODI	25	25	8
V_{ic}	100	100	97
P_0	100	100	89

There were a total of 36 sets of ROIs from six patients (Table 4). [a]Significant regions-of-interest (ROIs) are determined after multiple comparisons across 36 ROI sets and 8 MRI measures ($36 \times 8 = 288$) with a false discovery rate of less than 5% (*i.e.*, $q < 0.05$; Additional Table 1, Individual lesion level analyses). NAWM: Normal appearing white matter; ROI: region of interest; FLAIR: fluid attenuated inversion recovery; AD: Axial diffusivity; RD: radial diffusivity; MD: mean diffusivity; FA: fractional anisotropy; RD: radial diffusivity; ODI: orientation dispersion index; V_{ic}: volume fraction for intra-axonal water; P_0: q-space derived zero-displacement probability.

Table 6

Comparisons of diffusion parameters in the lesion, perilesion, and NAWM ROIs at the group level

Diffusion model	MRI measures	ROI	Mean	SD	$F_{(2,10)}$	P^a	P-value[b]		
							Lesion-perilesion	Lesion-NAWM	Perilesion-NAWM
DTI	AD (10^{-6} mm^2/s)	Lesion	1375	237					
		Perilesion	1167	67	8.4[c]	0.032	–	–	–
		NAWM	1093	36					
	RD (10^{-6} mm^2/s)	Lesion	848	236					
		Perilesion	583	34	11.8[c]	0.015	–	–	–
		NAWM	488	27					
	MD (10^{-6} mm^2/s)	Lesion	1024	236					
		Perilesion	778	42	11.2[c]	0.020	–	–	–
		NAWM	690	11					
	FA	Lesion	0.34	0.06					
		Perilesion	0.43	0.02	11.9	0.020	–	–	--
		NAWM	0.48	0.04					
NODDI	ODI	Lesion	0.28	0.04					
		Perilesion	0.27	0.03	0.32	0.742	–	–	–
		NAWM	0.28	0.02					
	V_{ic}	Lesion	0.45	0.08					
		Perilesion	0.59	0.04	39.7	0.002	0.012	0.001	0.004
		NAWM	0.70	0.04					
q-space	P_0	Lesion	0.56	0.11					
		Perilesion	0.73	0.03	31.4	0.004	0.002	0.002	0.015
		NAWM	0.86	0.04					

[a]Bold fonts indicate overall analysis of variance that were significant at the Bonferroni corrected critical threshold (P) of 0.007 (0.05/7 diffusion metrics). [b]Post-hoc t-test for pairwise comparisons between the three ROIs (lesion, selected perilesion, and NAWM). Bold fonts indicate comparisons that were significant at the Bonferroni corrected critical threshold (P) of 0.017 (0.05/3 pairs). [c]$F_{(1.1, 5.6)}$ after application of Greenhouse-Geisser adjustment for violation of sphericity. NAWM: Normal-appearing white matter; ROI: region of interest; DTI: diffusion tensor imaging; NODDI: neurite orientation dispersion and density imaging; AD: axial diffusivity; RD: radial diffusivity; MD: mean diffusivity; FA: fractional anisotropy; RD: radial diffusivity; ODI: orientation dispersion index; V_{ic}: volume fraction for intra-axonal water; P_0: q-space derived zero-displacement probability.

Figure 4
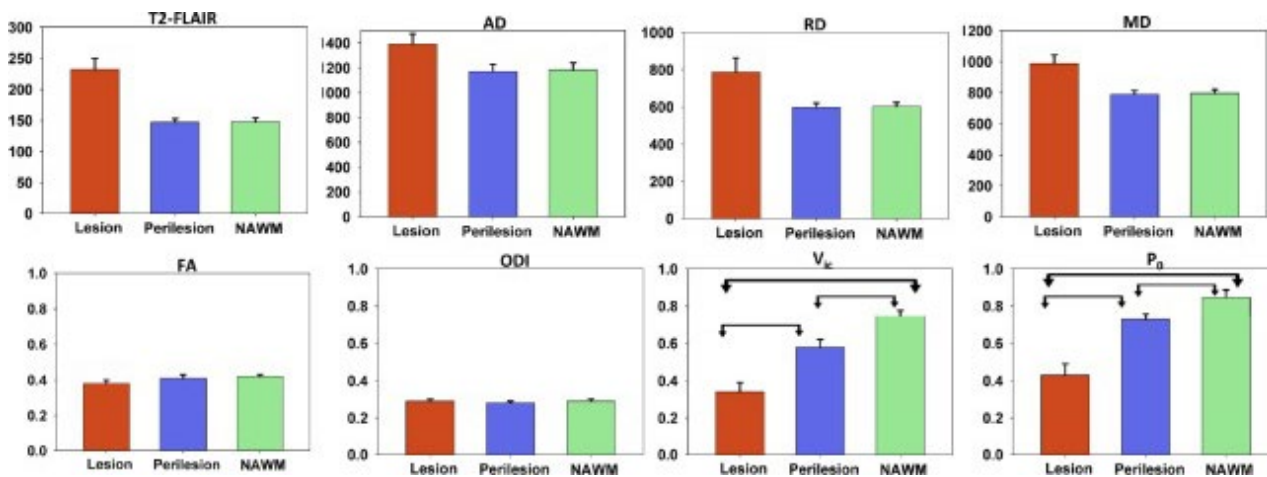
Bar plots of T2-FLAIR and diffusion metrics in the three types of ROIs.

The lesion, perilesion, and NAWM ROIs are color-coded in red, blue, and green, respectively. Error bars denote the standard deviation across 36 ROI sets. The overhead arrows denote significant differences in measurements between pairs of ROIs at a Bonferroni-corrected P threshold of 0.017 (Table 6). Note that T2-FLAIR intensity is not a quantitative measure; thus, it was not tested for statistical significance at the group level. FLAIR: Fluid attenuated inversion recovery; NAWM: normal-appearing white matter; ROIs: regions of interest.